

**Clinical feasibility of single-source dual-spiral 4D dual-energy CT for proton treatment planning within the thoracic region**

Wohlfahrt, P.; Troost, E. G. C.; Hofmann, C.; Richter, C.; Jakobi, A.;

Originally published:

July 2018

**International Journal of Radiation Oncology Biology Physics 102(2018)4, 830-840**

DOI: <https://doi.org/10.1016/j.ijrobp.2018.06.044>

Perma-Link to Publication Repository of HZDR:

<https://www.hzdr.de/publications/Publ-26550>

Release of the secondary publication  
on the basis of the German Copyright Law § 38 Section 4.

CC BY-NC-ND

1 **Title: Clinical feasibility of single-source dual-spiral 4D dual-energy CT for proton**  
2 **treatment planning within the thoracic region**

3  
4 **Shortened Running Title: Dual-spiral 4D-DECT for thoracic region**

5  
6 **ABSTRACT:**

7 **Purpose:** Single-source dual-spiral dual-energy computed tomography (DECT) provides  
8 additional patient information but is prone to motion between both consecutively acquired CT  
9 scans. Here, the clinical applicability of dual-spiral time-resolved DECT (4D-DECT) for  
10 proton treatment planning within the thoracic region was evaluated.

11  
12 **Methods and Materials:** Dual-spiral 4D-DECT scans of three lung-cancer patients were  
13 acquired. For temporally averaged datasets and 4 breathing phases, the geometrical  
14 conformity of 80/140kVp 4D-DECT scans before image post-processing was assessed by  
15 normalized cross correlation (NCC). Additionally, the conformity of the corresponding  
16 DECT-derived 58/79keV pseudo-monoenergetic CT datasets (MonoCTs) after image post-  
17 processing including deformable image registration (DIR) was determined. To analyze the  
18 reliability of proton dose calculation, clinical ( $Plan_{Clin}$ ) and artificial worst-case ( $Plan_{WorstCase}$ ,  
19 targeting diaphragm) treatment plans were calculated on 140kVp and 79keV datasets and  
20 compared with gamma analyses (0.1% dose-difference, 1mm distance-to-agreement  
21 criterion). The applicability of patient-specific DECT-based stopping-power-ratio (SPR)  
22 prediction was investigated and proton range shifts compared to the clinical heuristic CT-  
23 number-to-SPR conversion (HLUT) were assessed. Finally, the delineation variability of an  
24 experienced radiation oncologist was quantified on DECT-derived datasets.

26 **Results:** Dual-spiral 4D-DECT scans without DIR showed a high geometrical conformity  
27 with average NCC ( $\pm 1SD$ ) of 98.7( $\pm 1.0$ )% including all patient voxel or 88.2( $\pm 7.8$ )%  
28 considering only lung. DIR clearly improved the conformity leading to average NCC of  
29 99.9( $\pm 0.1$ )% and 99.6( $\pm 0.5$ )%, respectively. Plan<sub>Clin</sub> dose distributions on 140kVp and 79keV  
30 datasets were similar with average gamma passing rate of 99.9% (99.2%-100%). The worst-  
31 case evaluation still revealed high passing rates (average: 99.3%, minimum: 92.4%).  
32 Clinically relevant mean range shifts of 2.2( $\pm 1.2$ )% were determined between patient-specific  
33 DECT-based SPR prediction and HLUT. The intra-observer delineation variability could be  
34 slightly reduced by additional DECT-derived datasets.

35

36 **Conclusions:** 79keV MonoCT datasets can be consistently obtained from dual-spiral 4D-  
37 DECT and are applicable for proton dose calculation. Patient-specific DECT-based SPR  
38 prediction performed appropriately and potentially reduces range uncertainty in proton  
39 therapy of lung-cancer patients.

40 **MANUSCRIPT:**

41 **Introduction**

42 Compared to single-energy computed tomography (SECT), the acquisition of two CT scans  
43 with different x-ray spectra (dual-energy CT, DECT) provides additional patient information  
44 and allows for the generation of a variety of image datasets useful for reducing metal artifacts,  
45 increasing image quality, improving tumor delineation and radiotherapy planning (1–3). As  
46 recently demonstrated in biological tissues and an anthropomorphic phantom, DECT enables  
47 a reliable prediction of stopping-power ratio (SPR) eventually leading to reduced uncertainty  
48 margins in proton therapy (4–7).

49 Several technical options of DECT are currently available. With a dedicated dual-source  
50 DECT scanner, both CT scans are recorded simultaneously, but the DECT information is only  
51 available in a field of view (FOV) of 30–35 cm (8). To gather DECT data in a FOV of 50 cm,  
52 typically required for radiotherapy planning in anatomical regions such as thorax, abdomen or  
53 pelvis, the different CT datasets can be obtained consecutively (“dual-spiral”) by acquiring  
54 two separate CT scans one after the other, or almost simultaneously by continuous fast  
55 voltage switching, dual-layer detector or split-beam filter using a single-source CT scanner (2,  
56 9–11). From the single-source techniques, the dual-spiral DECT approach allows for an  
57 independent tube current modulation, a larger energy separation and can be performed by  
58 standard CT scanners with appropriate software. However, dual-spiral DECT is prone to  
59 uncertainties due to patient motion during imaging (e.g., breathing, swallowing, heartbeat,  
60 gastro-intestinal peristalsis), which leads to different anatomies in the subsequent CT scans.

61 In this study, the clinical feasibility of dual-spiral time-resolved (4D) DECT for proton  
62 treatment planning within the thoracic region, i.e. in the presence of respiratory motion, was  
63 analyzed using a single-source CT scanner. For this purpose, the geometrical similarity of  
64 both individual 4D-DECT scans and the impact of DECT-derived datasets on dose calculation  
65 were determined. In addition, the applicability of patient-specific DECT-based stopping-

66 power-ratio (SPR) prediction, aiming at more precise proton range estimation, and the intra-  
67 observer variability of tumor delineation on different DECT datasets were investigated.

68

## 69 **Methods and Materials**

### 70 *Patient data*

71 Three consecutive patients with advanced stage non-small-cell lung cancer (NSCLC, patient  
72 and tumor details in Table EAA, Supplement EA) participating in the phase II clinical trial  
73 XXX were selected in accordance with the approval of the local ethics committee XXX.  
74 Based on 4D-SECT scans, patient-specific internal gross tumor volumes (iGTVs) were  
75 defined by an experienced radiation oncologist. The clinical target volumes (CTVs)  
76 encompassed the iGTV and involved lymph nodes with 8 mm isotropic margin subsequently  
77 corrected for anatomical boundaries (Figure EAA(a), Supplement EA). Tumor motion was  
78 determined in cranio-caudal, left-right and anterior-posterior direction using the center-of-  
79 mass of the gross tumor volume (GTV) defined on each 4D-SECT respiratory phase (Table  
80 EAA, Supplement EA). Furthermore, the diaphragm motion was quantified based on the  
81 visible diaphragm line in exhalation and inhalation CT datasets.

82

### 83 *CT acquisition*

84 For treatment planning, 120 kVp 4D-SECT scans with  $1 \times 1 \times 2$  mm<sup>3</sup> voxel size were acquired  
85 at a single-source CT scanner SOMATOM Definition AS (Siemens Healthineers, Forchheim,  
86 Germany). An iterative reconstruction kernel with beam hardening correction concerning  
87 bone (Q34/5, SAFIRE) was applied to reduce image noise (adjusted by Siemens CARE  
88 Dose4D) and patient-size dependent CT number variations.

89 Respiratory motion during CT acquisition was recorded using a pressure belt system (ANZAI,  
90 Anzai Medical Co., Ltd, Tokyo, Japan) positioned onto the patient's abdomen. Four CT  
91 datasets representing different breathing phases (maximum and slopes of inhalation and

92 exhalation) were reconstructed using relative amplitude-based binning of CT projections  
93 according to the patient's breathing pattern. For a rotation time of 500 ms, this quick scan  
94 reconstruction results in a temporal resolution of approximately 250 ms for each respiratory  
95 phase per breathing period. Furthermore, a temporally averaged CT dataset was reconstructed  
96 using all CT projections.

97 To assess anatomical and motion changes during the course of treatment, these patients  
98 underwent weekly control 4D-SECT scans according to the clinical protocol. For the three  
99 selected patients, two dual-spiral 4D-DECT scans were acquired with similar total CT dose in  
100 between fractions 14-19 and 27-32, respectively. Each dual-spiral 4D-DECT scan comprises  
101 two 4D-SECT scans of 80 kVp and 140 kVp (Table EAB, Supplement EA), which were  
102 consecutively recorded within approximately 95 s each and a 10 s time delay for repositioning  
103 in between (Figure 1). Image reconstruction was performed as described previously using the  
104 same nominal relative amplitude-based binning.

105

#### 106 *4D-DECT image post processing*

107 The application syngo.CT DE Monoenergetic Plus of the Siemens image post-processing  
108 software syngo.via was applied on dual-spiral 4D-DECT scans to create pseudo-  
109 monoenergetic CT datasets (MonoCTs) of 58 keV, 79 keV and 170 keV. The 58/79 keV  
110 datasets comprised similar attenuation information as the initial 80/140 kVp CT scans, but  
111 were aligned by deformable image registration (DIR) and contained less image noise (2).  
112 Material parameters, such as relative electron density (RED), obtained from 170 keV  
113 MonoCT, and relative photon cross section (RCS), derived by dividing 79 keV MonoCT by  
114 RED, were determined and used to calculate SPR datasets (12). This patient-specific SPR  
115 prediction approach, referred to as RhoSigma, was implemented as described in XXX.

116

#### 117 *Treatment planning*

118 Passively scattered proton treatment plans with three fields were generated in XiO (Elekta  
 119 AB, Stockholm, Sweden) using the average planning SECT scan and the clinical heuristic  
 120 CT-number-to-SPR conversion (HLUT) of our institution (XXX). Average dose to the CTV  
 121 was aimed at 66 Gy(RBE) using a relative biological effectiveness (RBE) of 1.1. For  
 122 hardware preparation and range/modulation determination, the iGTV was assigned to a mean  
 123 density derived from the GTV of each 4D-SECT breathing phase. Treatment uncertainty was  
 124 included in aperture margins and compensator smearing of 10 mm as well as range  
 125 uncertainty of (3.5% + 2 mm). Dose calculations were performed without density assignment  
 126 to the iGTV using a  $1 \times 1 \times 1$  mm<sup>3</sup> dose grid and a pencil-beam algorithm.  
 127 Additionally, worst-case-scenario plans were generated using a single lateral proton beam  
 128 covering an artificial target volume that encompassed the diaphragm, the anatomical region  
 129 where the highest motion occurred (Figure EAA(b), Supplement EA).

130

131 *4D-DECT scan similarity*

132 The geometrical similarity of dual-spiral DECT datasets was assessed visually and by  
 133 normalized cross correlation (NCC)

$$\text{NCC} = \frac{\sum_{\text{ROI}} H_i H_j}{\sqrt{\sum_{\text{ROI}} H_i^2 \sum_{\text{ROI}} H_j^2}} \cdot 100\% \quad (1)$$

134 including CT numbers of both datasets,  $H_i$  and  $H_j$ , within region of interests (ROIs), *e.g.*,  
 135 patient body, CTV, heart and total lung. NCC of 100% declares perfect agreement and 0% no  
 136 conformity.

137 To analyze patient datasets of different x-ray attenuation, CT numbers of 80 kVp/58 keV were  
 138 transferred to 140 kVp/79 keV using a linear conversion table established on a DECT scan of  
 139 a rigid thorax phantom (Figure EBA, Supplement EB). Subsequently, NCC values were  
 140 determined for 4D-DECT datasets before (80/140 kVp) and after (58/79 keV) DIR. The  
 141 sensitivity of NCC was estimated by comparing a patient dataset shifted by 1, 2, 3, 5, 7,

142 10 mm in cranio-caudal direction with the non-shifted dataset to correlate geometrical  
143 deviation with NCC (Table EBA, Figure EBB Supplement EB). Furthermore, breathing  
144 patterns during dual-spiral 4D-DECT were compared with regard to their variability and the  
145 feasibility to identify differences in DECT scans.

146

#### 147 *Reliability of 79 keV MonoCT*

148 To assess the influence of anatomical changes in between both 4D-DECT scans on dose  
149 calculation, the clinical and worst-case-scenario plans were recalculated on DECT-derived  
150 79 keV MonoCT datasets and their associated 140 kVp SECT scans as reference in  
151 RayStation 6.0 (RaySearch Laboratories, Stockholm, Sweden) using the clinical HLUT  
152 (XXX). For average CT datasets and four breathing phases, differences in dose distributions  
153 were quantified by voxelwise dose deviations and two-dimensional gamma analysis with  
154 1 mm distance-to-agreement and 0.1% dose-difference,  $\gamma(1\text{mm},0.1\%)$ , or 1% dose-  
155 difference criterion,  $\gamma(1\text{mm},1\%)$ , respectively (13). Furthermore, deviations in dose-volume  
156 histograms (DVHs) were evaluated for CTV and the organs at risk (OARs) heart, esophagus  
157 and total lung.

158

#### 159 *Application of patient-specific DECT-based SPR prediction*

160 Since a direct import of SPR datasets for dose calculation in RayStation 6.0 is not possible,  
161 XiO was used to recalculate clinical treatment plans on (a) 79 keV MonoCT datasets applying  
162 the clinical HLUT and (b) SPR datasets derived by RhoSigma. Deviations in dose distribution  
163 were evaluated as described above for average CT datasets and breathing phases. To assess  
164 water-equivalent range shifts ( $\Delta R_{\text{WET}}$ ) between the RhoSigma and HLUT approach, depth-  
165 dose curves in beam direction traversing the CTV with 1 mm spacing were analyzed for each  
166 treatment field using an in-house implemented ray-tracing algorithm (XXX). For this purpose,  
167 the distal range at 80% of the reference dose was used as proton range.

168 For average CT datasets, the correlation of CT number and SPR obtained from RhoSigma  
169 were determined within the irradiated volume (20% isodose) and illustrated as frequency  
170 distribution (Figure 4b).

171

### 172 *Tumor delineation using DECT*

173 To analyze the impact of image contrast on tumor detection, an experienced radiation  
174 oncologist delineated the GTV of each patient on several average CT datasets. First, only the  
175 79 keV MonoCT dataset was used, which represents the clinical standard procedure. In a  
176 second step, the RED and RCS datasets were jointly provided. To quantify the intra-observer  
177 variability, the delineations were repeated once after a week. The conformity of GTV  
178 contours was assessed by Jaccard index and Hausdorff distance defined as 95<sup>th</sup> quantile of  
179 distances for each patient (14, 15).

180

## 181 **Results**

### 182 *Similarity of dual-spiral 4D-DECT*

183 Only small differences were found between the dual-spiral 80/140 kVp 4D-DECT scans,  
184 which are mainly visible on the upper anterior thorax wall and are in accordance with the  
185 assessed variability of the breathing amplitudes (Figure ECA, Supplement EC). Changes in  
186 respiratory frequency were rather minor and virtually adjusted in image reconstruction. For  
187 average CT datasets, the patient body, CTV and heart revealed a NCC > 99.5% and both  
188 lungs a NCC > 95% (Table 1), indicating mean shifts between each scan equivalent to global  
189 shifts of less than 0.5 mm (Table EBA, Supplement EB). CT datasets of individual breathing  
190 phases showed slightly less similarity and the respective NCC corresponded to shifts of  
191 approximately 1 mm. This confirms the general high resemblance of dual-spiral 4D-DECT  
192 scans. NCC values for all patients and ROIs are given in Tables EBB-EBE, Supplement EB.

193 Patient movement had a larger impact than breathing: In one case, the patient had to cough  
194 considerably at the end of the first 4D-DECT scan, which changed his overall body position  
195 especially visible by an altered position of the vertebrae. The NCC dropped markedly to  
196 98.7% for body and 88.4% for total lung, similar to a global shift of approximately 1.3 mm  
197 between the average 80/140 kVp datasets.

198 The differences caused by respiratory motion could almost be completely resolved by DIR,  
199 which was applied between 80/140 kVp datasets prior to further image post-processing. This  
200 resulted in increased NCC values between 58/79keV datasets, indicating shifts less than 0.1  
201 mm, also for the coughing patient (Table 1, Figure 2).

202 In contrast, movement of other organs or structures, *e.g.* the esophagus or gas in the stomach,  
203 and irregularities in respiratory motion visible at the diaphragm could not be sufficiently  
204 corrected by DIR and led to remaining uncertainties in DECT-derived datasets. Since these  
205 volumes were quite small, they did not influence the NCC, but were well visible as bright  
206 artifacts in DECT-derived datasets, such as RED and SPR (Figure EDA, Supplement ED).

207

#### 208 *Feasibility of dose calculation on 79 keV MonoCT datasets*

209 Dose distributions calculated on 140 kVp and DECT-derived 79 keV MonoCT datasets were  
210 highly similar leading to no differences in DVH parameters of OARs and CTV. For clinical  
211 treatment plans, maximum dose differences ranged between 0.2-0.6 Gy(RBE) resulting in  
212  $\gamma(1\text{mm},1\%) = 100\%$  for all average CT datasets and breathing phases. Even the tighter  
213 gamma criterion revealed average and minimum gamma passing rates of  $\gamma_{\text{avg}}(1\text{mm},0.1\%) =$   
214  $99.9\%$  and  $\gamma_{\text{min}}(1\text{mm},0.1\%) = 99.2\%$ .

215 Dose differences of up to 2.2 Gy(RBE) were obtained for worst-case scenarios, which led to  
216 remainingly high gamma passing rates of  $\gamma_{\text{avg}}(1\text{mm},0.1\%) = 99.3\%$ ,  $\gamma_{\text{min}}(1\text{mm},0.1\%) =$   
217  $92.4\%$  and  $\gamma_{\text{min}}(1\text{mm},1\%) = 98.0\%$ . DVH parameters of OARs and CTV did not change.

218

219 *Application of patient-specific DECT-based SPR prediction*

220 Dose distributions calculated on 79 keV MonoCT and SPR datasets derived by RhoSigma  
221 revealed dose differences of up to 21.2 Gy(RBE) and an average gamma passing rate of  
222  $\gamma_{\text{avg}}(1\text{mm},1\%) = 82.8\%$ . Overall and field-specific dose differences and their associated  
223 water-equivalent range shifts are illustrated in Figure 3. The impact on DVH parameters  
224 depended on patient anatomy and beam direction. The volume of the contralateral lung  
225 receiving 5 Gy(RBE) increased by 4% for one patient with one beam exiting into this region  
226 (Figure 3b), while the other two patients showed smaller changes of 1.5% and 0%,  
227 respectively. Target coverage, defined by the dose applied to 98% of the CTV, remained  
228 stable for all patients with reductions of only 0.1%, which demonstrates the robustness of the  
229 treatment planning approach against CT calibration uncertainty.

230 Considering all investigated depth-dose profiles obtained for all 4D-DECT datasets of each  
231 patient, a mean relative water-equivalent range shift ( $\pm$  standard deviation) of 2.2% ( $\pm 1.2\%$ )  
232 between the RhoSigma and HLUT approach was determined (Figure 4c). This corresponds to  
233 a mean absolute water-equivalent range shift of 2.9 mm ( $\pm 1.4$  mm). These deviations were  
234 mainly caused by the HLUT which predicts larger SPR for muscles ( $H \approx 40$  HU), trabecular  
235 bone ( $100 \text{ HU} \leq H \leq 300 \text{ HU}$ ) and tissue mixtures with CT numbers ranging from  $-400$  HU  
236 to  $100$  HU (Figure 4b). Accordingly, range shifts within a treatment field depend on the  
237 distribution of tissues traversed in beam direction and result in an intra-patient variability of  
238 1.1%, which is clearly larger than the inter-patient variation of 0.1% (Figure 4a). Furthermore,  
239 range shifts were similar using the average CT dataset (2.3%) or a breathing phase (2.2%) for  
240 dose calculation.

241

242 *GTV delineation*

243 The intra-observer variability of GTV delineation could be slightly reduced by jointly using  
244 DECT-derived RED and RCS datasets rather than only the 79 keV MonoCT dataset (Figure

245 5). This was indicated by an increased mean Jaccard index ( $\pm$  standard deviation) of  
246 82.6% ( $\pm 2.1\%$ ) compared to 80.3% ( $\pm 4.9\%$ ) and reduced mean Hausdorff distance of  
247 3.8 mm ( $\pm 1.1$  mm) compared to 4.5 mm ( $\pm 0.8$  mm).

248 The GTV contours (fusion of repeated delineations) obtained on 79 keV MonoCT or  
249 RED/RCS datasets revealed a mean Jaccard index of 82.8% ( $\pm 4.2\%$ ) and Hausdorff distance  
250 of 3.9 mm ( $\pm 0.5$  mm).

251

## 252 **Discussion**

253 The presented study demonstrated the feasibility of dual-spiral 4D-DECT for radiotherapy  
254 planning in the thoracic region in terms of anatomical and dosimetrical consistency and  
255 outlined the large variety of possibilities for potentially improving tumor delineation and CT-  
256 based SPR prediction in proton therapy. This approach assumes a high similarity in motion  
257 and anatomy between both consecutive 4D-DECT scans. Guckenberger *et al.* (16)  
258 demonstrated that multiple 4D-SECT scans acquired within a 30 minute timeframe are  
259 equally representative for treatment planning for the majority of patients. Malinowski *et al.*  
260 (17) and Shah *et al.* (18) showed that relevant changes in respiratory motion usually occur  
261 after a longer time period as opposed to that required for dual-spiral 4D-DECT. For the  
262 patients investigated in the presented study, the differences between both 4D-DECT scans  
263 were found to be small. This allows for reliable image post-processing and eventually clinical  
264 application of dual-spiral 4D-DECT. Thus, as recently shown for brain-tumor and prostate-  
265 cancer patients (3), patient-specific DECT-based SPR prediction is also clinically feasible  
266 within the thoracic region.

267 4D-DECT provides more detailed patient information of crucial importance for three aspects  
268 of proton therapy. First, patient-specific SPR predictions consider tissue heterogeneity and  
269 patient variability, which cannot be adequately incorporated using the clinical state-of-the-art  
270 HLUT approach, and thus can lead to more reliable dose calculation in proton treatment

271 planning (19, 20). The impact of using a pencil-beam dose algorithm instead of a more  
272 sophisticated Monte Carlo approach, which limits the precision of the presented dose  
273 calculations in heterogeneous anatomical regions as thorax (21), remains small in relative  
274 dose comparisons and would not change the conclusions we draw here.

275 Second, multiple datasets of different image contrast can be derived from DECT, which might  
276 support a more reliable target delineation. For the evaluated NSCLC patient cohort, the intra-  
277 observer variability of GTV delineation was slightly influenced by different DECT datasets.  
278 To finally judge the effect on delineation precision, a further comprehensive evaluation  
279 should include more patients, more physicians to assess the inter-observer variability and  
280 additional DECT-derived datasets to obtain optimal settings. As delineation of lung tumors is  
281 supposed to be rather robust owing to the large CT image contrast to surrounding tissues, such  
282 a study should also be extended to other tumor entities to analyze site-specific advantages.

283 Third, information about motion variability can be gained. Differences in breathing pattern  
284 over time are a general challenge in radiotherapy, where a 4D-SECT scan acquired days to  
285 weeks before treatment is used as single baseline for therapy. The comparison of the two CT  
286 datasets of a dual-spiral 4D-DECT scan can contribute to identify patients with irregular and  
287 non-representative breathing patterns or to illustrate esophageal motion and regions of severe  
288 gastro-intestinal peristalsis during CT acquisition. These patients might currently not be  
289 eligible for accurate DECT-based SPR prediction. However, since SPR datasets visualize  
290 regions of severe motion, an additional image-based algorithm can be developed in future to  
291 detect such motion-induced changes and consider them in SPR prediction. Even if too large  
292 differences occur during dual-spiral 4D-DECT acquisition, hampering the calculation of  
293 reliable DECT-based datasets, still important information about motion variability and  
294 reliability regarding iGTV delineation for treatment planning can be gathered. Both  
295 consecutive 4D-DECT scans could also be included in robust optimization techniques  
296 including breathing variability in treatment planning (22–24). Furthermore, this could also

297 highlight patients, who may require the application of a breathing suppression technique, a  
298 close intra-therapeutic monitoring to ensure short-term plan adaptations or even real-time  
299 imaging during treatment (25). Standard SECT-based dose calculation can always be  
300 performed without limitations using only the 140 kVp dataset. Thus, DECT scans of patients  
301 will always provide additional information without being disadvantageous for the individual  
302 patient.

303 In this proof-of-principle study, only six 4D-DECT scans of three advanced stage NSCLC  
304 patients with small tumor motion were investigated. As most advanced stage NSCLC tumors  
305 do not move significantly (26), the presented results will be valid for the majority of these  
306 patients. A comprehensive analysis of 4D-DECT is currently planned including more patients  
307 with larger tumor motion, which may have a larger impact on dose calculation as shown for  
308 the diaphragm region.

309

### 310 **Conclusions**

311 Single-source dual-spiral DECT can be reliably combined with time-resolved image  
312 acquisition, which results in 4D-DECT applicable for proton treatment planning within the  
313 thoracic region. Motion-induced changes in patient anatomy between the acquisition of both  
314 4D-DECT scans are effectively minimized by deformable image registration allowing for a  
315 consistent DECT-based SPR prediction. Remaining motion artifacts in SPR datasets due to  
316 unstable breathing patterns indicate potential uncertainties during treatment, which can be  
317 considered in treatment planning using both 4D-DECT datasets individually.

318 **REFERENCES**

- 319 1. van Elmpt W, Landry G, Das M, *et al.* Dual energy CT in radiotherapy: Current  
320 applications and future outlook. *Radiother. Oncol.* 2016;119:137–144.
- 321 2. Wohlfahrt P, Möhler C, Hietschold V, *et al.* Clinical implementation of dual-energy CT for  
322 proton treatment planning on pseudo-monoenergetic CT scans. *Int. J. Radiat. Oncol. Biol.*  
323 *Phys.* 2017;97:427–434.
- 324 3. Wohlfahrt P, Möhler C, Stützer K, *et al.* Dual-energy CT based proton range prediction in  
325 head and pelvic tumor patients. *Radiother. Oncol.* 2017;125:526–533.
- 326 4. Taasti VT, Michalak GJ, Hansen DC, *et al.* Validation of proton stopping power ratio  
327 estimation based on dual energy CT using fresh tissue samples. *Phys. Med. Biol.* 2017.
- 328 5. Bär E, Lalonde A, Zhang R, *et al.* Experimental validation of two dual-energy CT methods  
329 for proton therapy using heterogeneous tissue samples. *Med. Phys.* 2017.
- 330 6. Möhler C, Russ T, Wohlfahrt P, *et al.* Experimental verification of stopping-power  
331 prediction from single- and dual-energy computed tomography in biological tissues. *Phys.*  
332 *Med. Biol.* 2018.
- 333 7. Wohlfahrt P, Möhler C, Richter C, *et al.* Evaluation of Stopping-Power Prediction by Dual-  
334 and Single-Energy Computed Tomography in an Anthropomorphic Ground-Truth Phantom.  
335 *Int. J. Radiat. Oncol.* 2018;100:244–253.
- 336 8. Flohr TG, McCollough CH, Bruder H, *et al.* First performance evaluation of a dual-source  
337 CT (DSCT) system. *Eur. Radiol.* 2006;16:256–268.
- 338 9. Kalender WA, Perman WH, Vetter JR, *et al.* Evaluation of a prototype dual-energy  
339 computed tomographic apparatus. I. Phantom studies. *Med. Phys.* 1986;13:334–339.
- 340 10. Heismann BJ, Wirth S, Janssen S, *et al.* Technology and image results of a spectral CT  
341 system. *Med. Imaging 2004 Phys. Med. Imaging, Pts 1 2.* 2004;5368:52–59.
- 342 11. Almeida IP, Schyns LEJR, Öllers MC, *et al.* Dual-energy CT quantitative imaging: a  
343 comparison study between twin-beam and dual-source CT scanners. *Med. Phys.* 2017;44:171–

- 344 179.
- 345 12. Möhler C, Wohlfahrt P, Richter C, *et al.* Range prediction for tissue mixtures based on  
346 dual-energy CT. *Phys. Med. Biol.* 2016;61:N268–N275.
- 347 13. Low DA, Harms WB, Mutic S, *et al.* A technique for the quantitative evaluation of dose  
348 distributions. *Med. Phys.* 1998;25:656–61.
- 349 14. Jaccard P. The distribution of the flora in the alpine zone. *New Phytol.* 1912;XI:37–50.
- 350 15. Taha AA, Hanbury A. Metrics for evaluating 3D medical image segmentation: analysis,  
351 selection, and tool. *BMC Med. Imaging.* 2015;15:29.
- 352 16. Guckenberger M, Wilbert J, Meyer J, *et al.* Is a Single Respiratory Correlated 4D-CT  
353 Study Sufficient for Evaluation of Breathing Motion? *Int. J. Radiat. Oncol. Biol. Phys.*  
354 2007;67:1352–1359.
- 355 17. Malinowski K, McAvoy TJ, George R, *et al.* Incidence of changes in respiration-induced  
356 tumor motion and its relationship with respiratory surrogates during individual treatment  
357 fractions. *Int. J. Radiat. Oncol. Biol. Phys.* 2012;82:1665–1673.
- 358 18. Shah C, Grills IS, Kestin LL, *et al.* Intrafraction variation of mean tumor position during  
359 image-guided hypofractionated stereotactic body radiotherapy for lung cancer. *Int. J. Radiat.*  
360 *Oncol. Biol. Phys.* 2012;82:1636–1641.
- 361 19. Yang M, Virshup G, Clayton J, *et al.* Theoretical variance analysis of single- and dual-  
362 energy computed tomography methods for calculating proton stopping power ratios of  
363 biological tissues. *Phys. Med. Biol.* 2010;55:1343–1362.
- 364 20. Wohlfahrt P, Möhler C, Greilich S, *et al.* Comment on: Dosimetric comparison of  
365 stopping-power calibration with dual-energy CT and single-energy CT in proton therapy  
366 treatment planning [Med. Phys. 43(6), 2845-2854 (2016)]. *Med. Phys.* 2017;44:5533–5536.
- 367 21. Grassberger C, Daartz J, Dowdell S, *et al.* Quantification of proton dose calculation  
368 accuracy in the lung. *Int. J. Radiat. Oncol. Biol. Phys.* 2014;89:424–430.
- 369 22. Li H, Zhang X, Park P, *et al.* Robust optimization in intensity-modulated proton therapy

370 to account for anatomy changes in lung cancer patients. *Radiother. Oncol.* 2015;114:367–372.

371 23. Van Der Voort S, Van De Water S, Perkó Z, *et al.* Robustness Recipes for Minimax

372 Robust Optimization in Intensity Modulated Proton Therapy for Oropharyngeal Cancer

373 Patients. *Int. J. Radiat. Oncol. Biol. Phys.* 2016;95:163–170.

374 24. Stützer K, Lin A, Kirk M, *et al.* Superiority in Robustness of Multifield Optimization

375 Over Single-Field Optimization for Pencil-Beam Proton Therapy for Oropharynx Carcinoma:

376 An Enhanced Robustness Analysis. *Int. J. Radiat. Oncol.* 2017;99:738–749.

377 25. Péguet N, Ozsahin M, Zeverino M, *et al.* Apnea-like suppression of respiratory motion:

378 First evaluation in radiotherapy. *Radiother. Oncol.* 2016;118:220–226.

379 26. Li Y, Kardar L, Li X, *et al.* On the interplay effects with proton scanning beams in stage

380 III lung cancer. *Med. Phys.* 2014;41:21721.

381

382 **TABLES**

383 **Table 1:** NCC values for the investigated lung-cancer patient cohort.

<b>Mean normalized correlation coefficient (NCC) <math>\pm</math> 1 standard deviation* / %</b>				
<b>80 kVp vs 140 kVp</b>				
	Average CT		CT Phases	
	Body	Lungs	Body	Lungs
Patient cohort <sup>#</sup>	99.64 $\pm$ 0.09	97.36 $\pm$ 0.57	98.90 $\pm$ 0.15	89.09 $\pm$ 3.05
Coughing patient	97.26	88.35	96.42 $\pm$ 0.08	72.47 $\pm$ 6.37
<b>58 keV vs 79 keV</b>				
	Average CT		CT Phases	
	Body	Lungs	Body	Lungs
Patient cohort <sup>#</sup>	99.90 $\pm$ 0.02	99.84 $\pm$ 0.03	99.85 $\pm$ 0.04	99.61 $\pm$ 0.15
Coughing patient	99.80	99.80	99.59 $\pm$ 0.15	98.97 $\pm$ 0.70

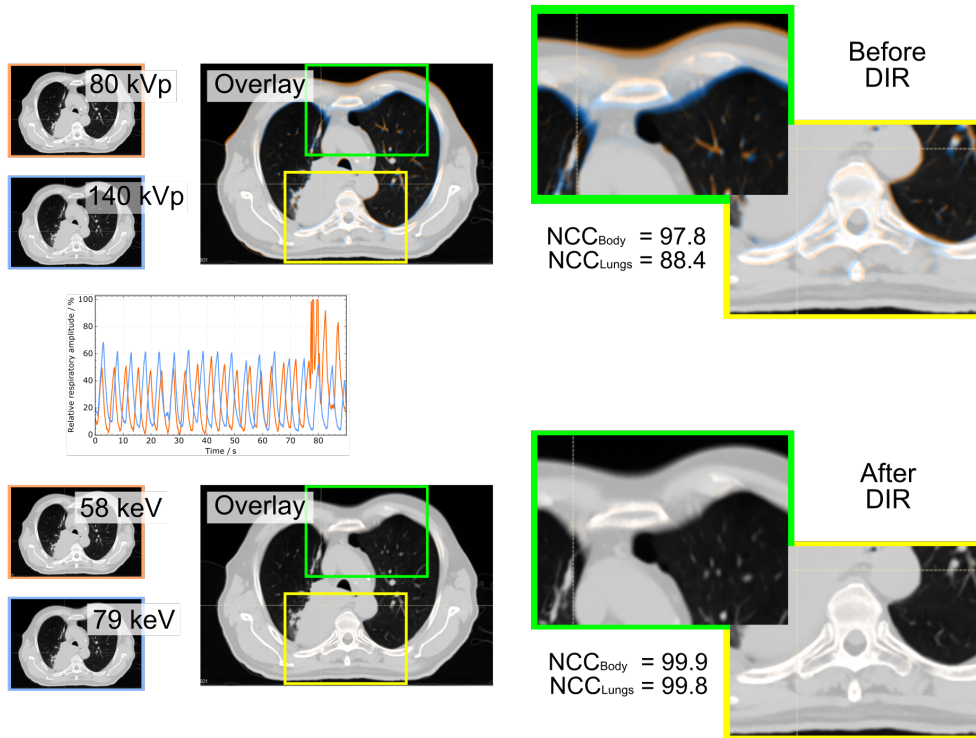
384 \* determined independent from the individual patient

385 <sup>#</sup> except for the dual-energy CT dataset of the coughing patient

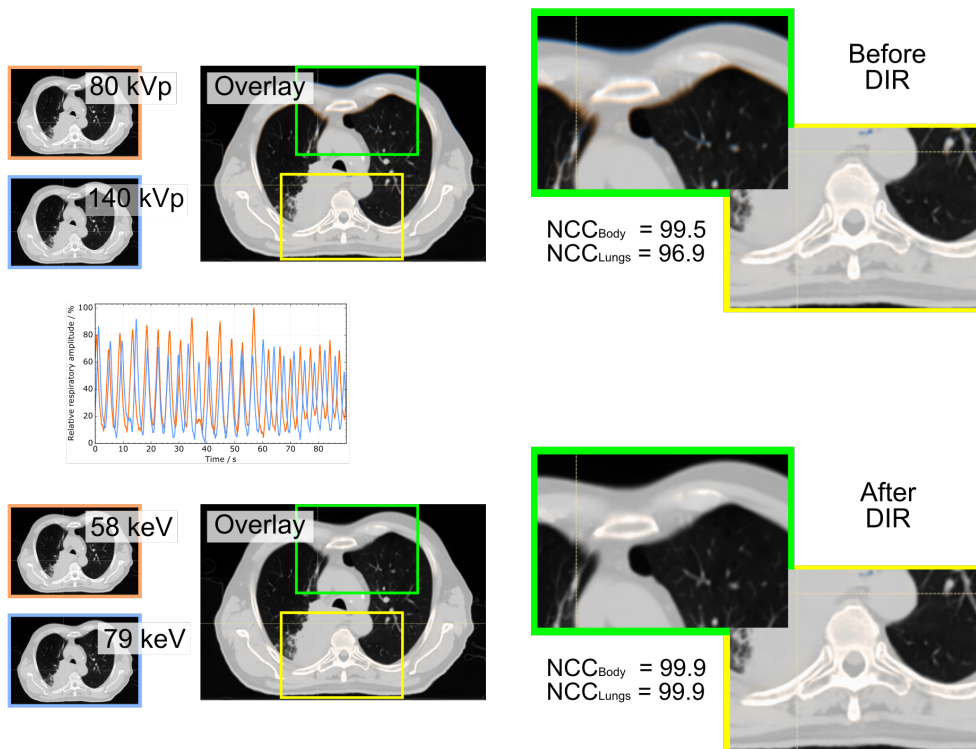
386



(a) Patient 2, 4D dual-energy CT scan 1, fraction 19



(b) Patient 2, 4D dual-energy CT scan 2, fraction 31

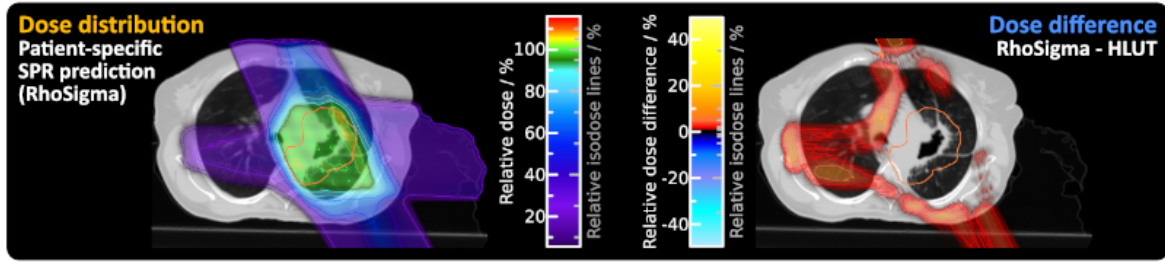


391

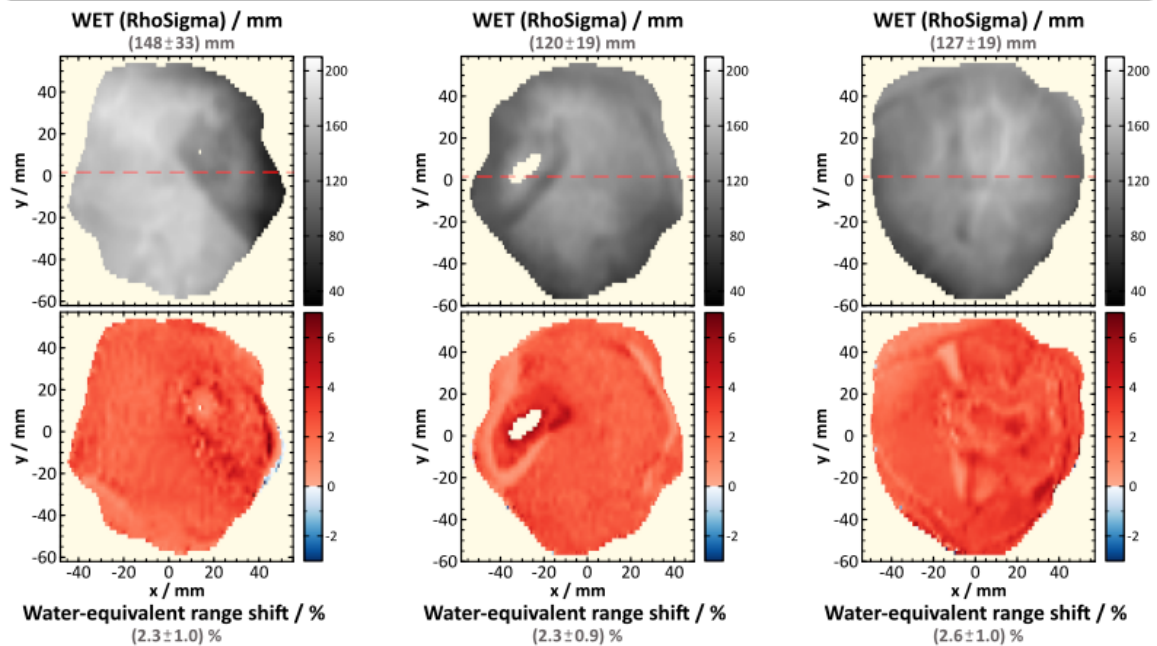
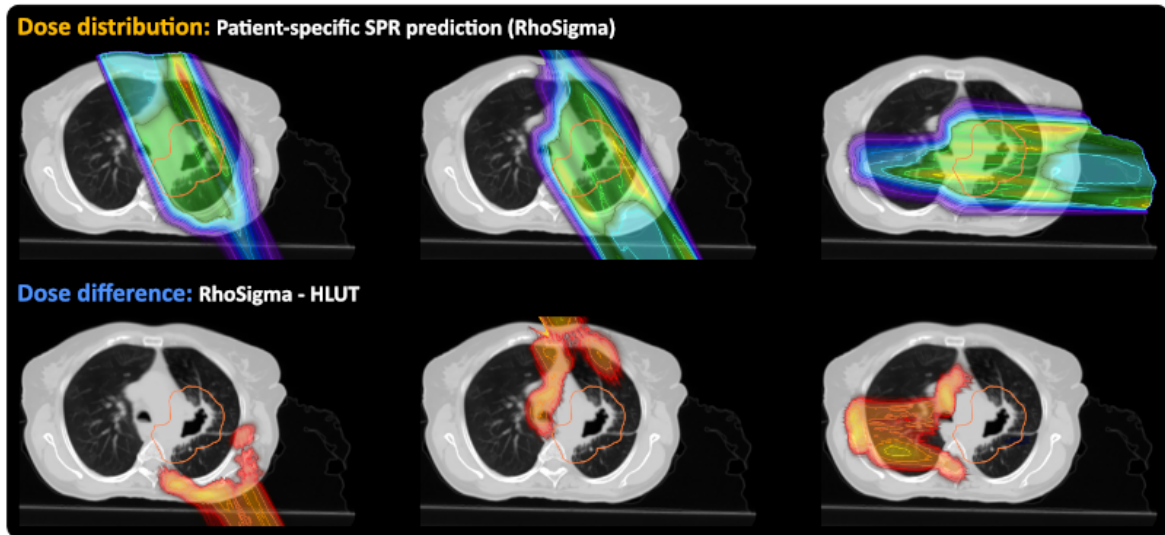
392 **Figure 2:** Dual-spiral 4D-DECT datasets of patient 2 before and after deformable image

393 registration (DIR).

(a) Overall treatment



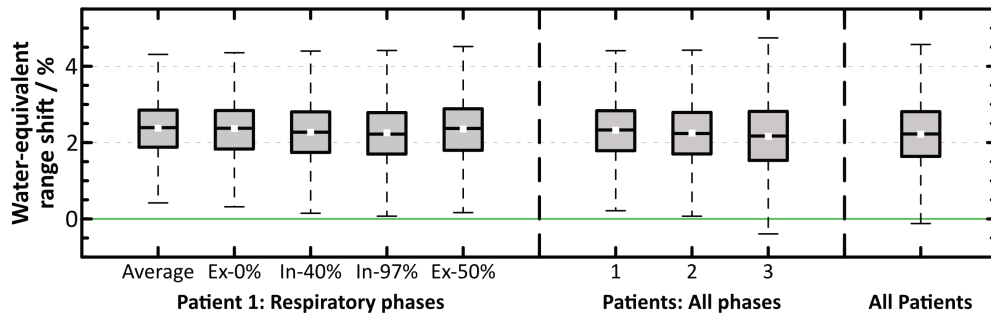
(b) Single treatment fields



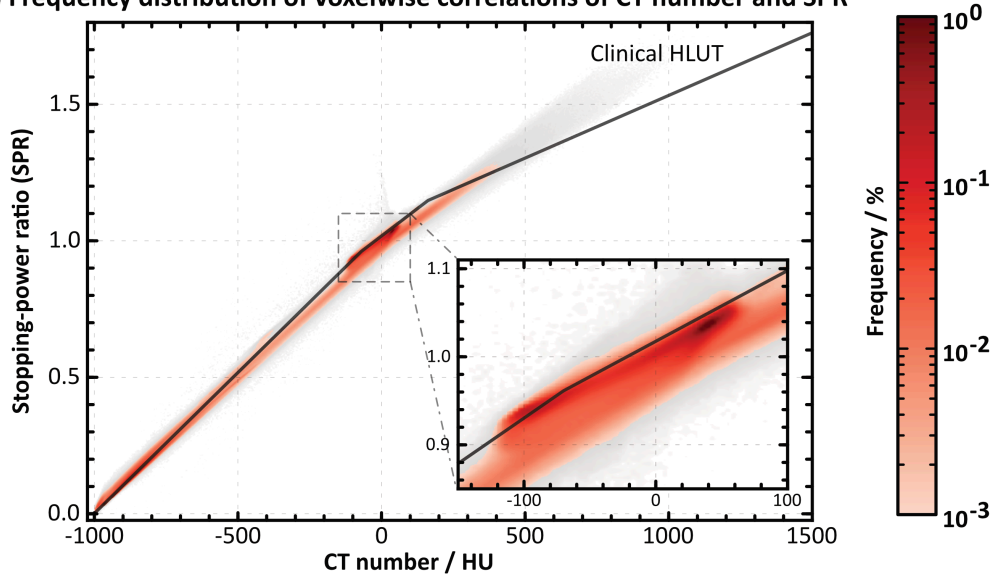
394

395 **Figure 3:** Dose distribution and difference between patient-specific prediction of stopping-  
 396 power ratio (SPR) and Hounsfield look-up table (HLUT) for (a) the overall treatment and (b)  
 397 single treatment fields of patient 1. Assessment of water-equivalent thickness and relative  
 398 range shifts in beam direction for each treatment field. (Mean  $\pm$  standard deviation) is stated  
 399 for each beam's eye view (BEV). The red dashed line indicates the axial CT slice in BEV.

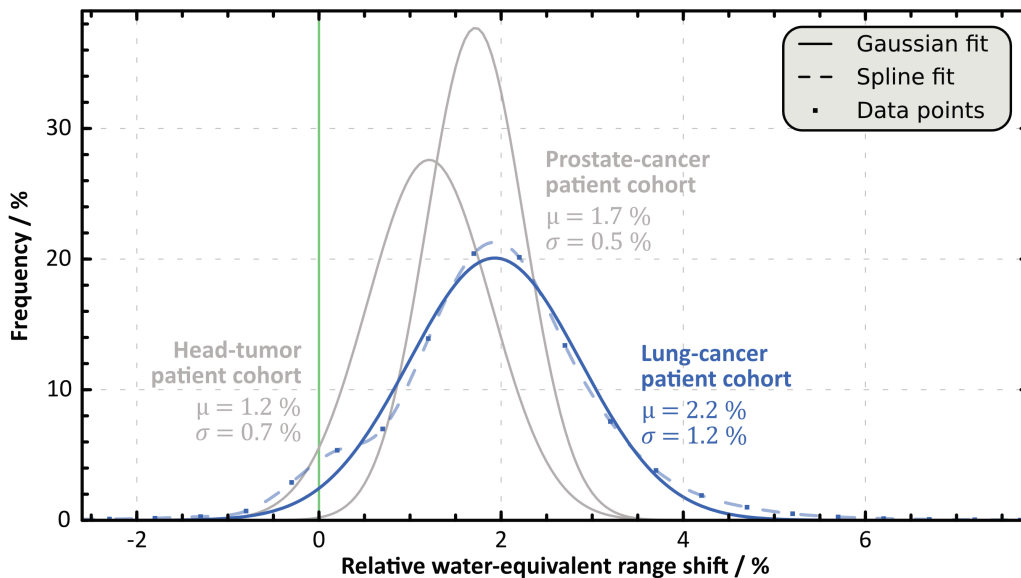
(a) Water-equivalent range shifts and deviations in stopping-power ratio (SPR) between patient-specific SPR prediction (RhoSigma) and Hounsfield look-up table (HLUT)



(b) Frequency distribution of voxelwise correlations of CT number and SPR



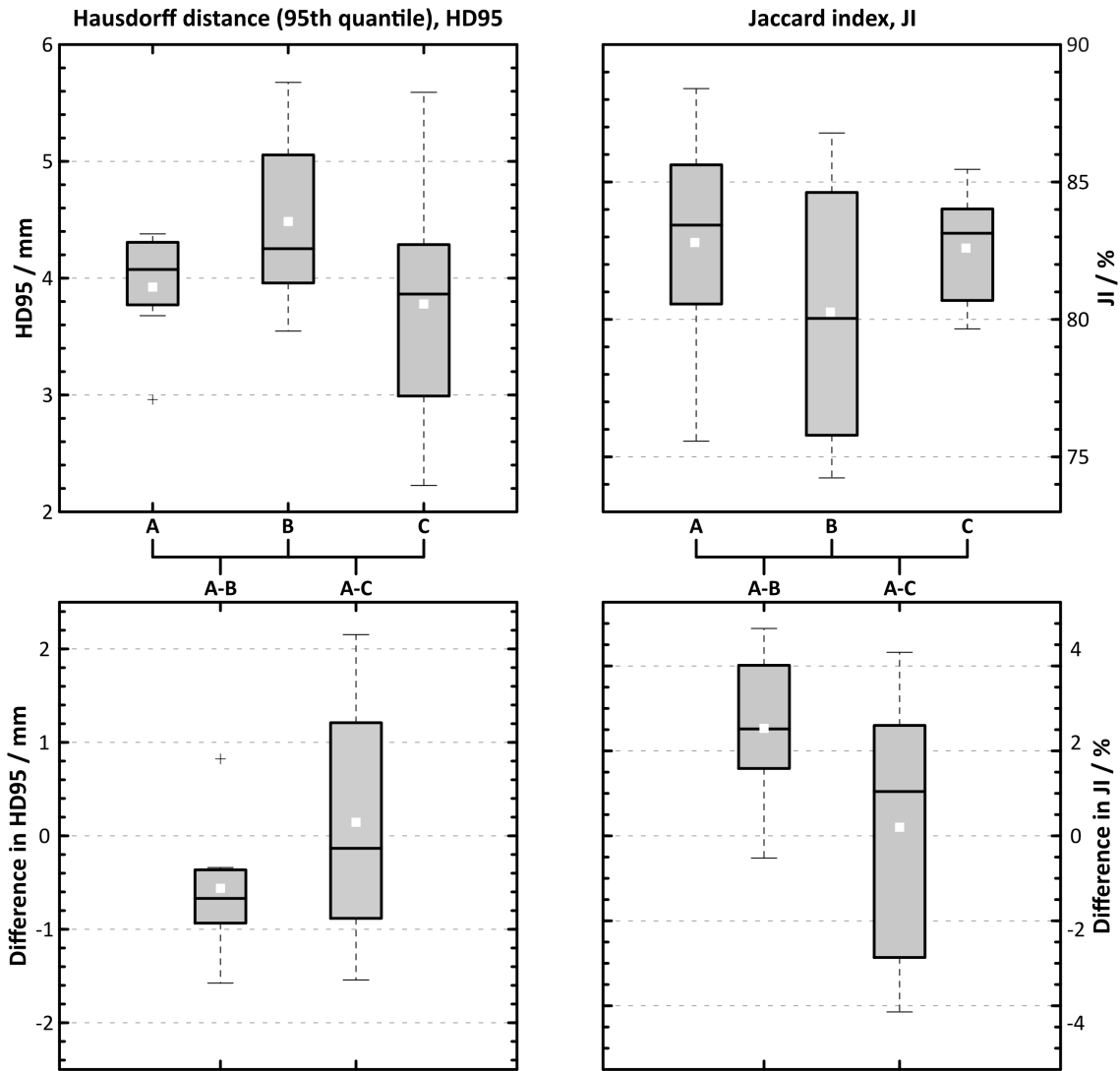
(c) Distribution of relative water-equivalent range shifts including all depth-dose profiles with mean difference  $\mu$  and standard deviation  $\sigma$



400

401 **Figure 4:** Water-equivalent range shifts and SPR distribution. Additionally, range shifts

402 obtained in head-tumor and prostate-cancer patients were illustrated (3).



- A ... Inter-modality variability between 79 keV pseudo-monoenergetic CT datasets (MonoCT) and a combination of relative-electron-density (RED) and 79 keV relative-cross-section (RCS) datasets. Repeated contours of the gross tumor volume (GTV) were fused.
- B ... Intra-observer variability on 79 keV MonoCT datasets
- C ... Intra-observer variability on a combination of RED and 79 keV RCS datasets

403

404 **Figure 5:** Intra-observer variability of GTV delineation.